Acta Mech 235, 3463–3481 (2024)
https://doi.org/10.1007/s00707-024-03902-5

ORIGINAL PAPER

Gongye Zhang · Xueqian Kong · Changwen Mi

Mechanically manipulated in-plane electric currents and thermal control in piezoelectric semiconductor films

Received: 24 December 2023 / Revised: 31 January 2024 / Accepted: 8 February 2024 / Published online: 13 March 2024

Abstract This study explores the new findings of in-plane mechanical forces on electric currents and thermal control in piezoelectric semiconductors. The thermo-electro-elastic theory is considered based on the thermo-piezoelectricity theory and drift–diffusion theory for semiconductors. A two-dimensional nonlinear model for in-plane deformations of piezoelectric semiconductor films is developed, where thermo-elastic, pyroelectric and thermoelectric couplings are involved. The newly developed nonlinear equations are directly solved based on the finite element method, while linearized equations derived from the nonlinear theory and corresponding analytical solutions are also obtained as a reference for validation. Our findings indicate that the in-plane mechanical forces exerted on piezoelectric semiconductors significantly influence both currents and thermal fluxes through piezoelectric coupling. Specifically, the angle of in-plane mechanical force relative to the c-axis significantly impacts the currents, with the potential to suppress, enhance or alter the direction, thereby affecting the temperature field. Based on these findings, an application simulation that focuses on mechanically induced current manipulation and thermal control is introduced and realized.

1 Introduction

During the past few decades, a substantial interest has existed in piezoelectric semiconductors (PSs). Semiconductors based on functional piezoelectric materials have facilitated widespread applications in energy harvesting and biomedicine [1–4]. Benefiting from the advantages of low-cost, high-energy conversion efficiency, as well as being environmentally friendly, applications of PSs like smart wearable electronics, portable electronic devices and self-powered sensors are generally used in people's daily life [5–8]. Studies on new high-performance composite materials and structural design with high efficiency have been analyzed by many researchers [9–14]. In PSs, the built-in potential barriers modulated by mechanical loads can effectively manipulate the charge transport behaviors [15–17]. Multi-couplings of piezoelectric and semiconductor materials have created a new research field called piezotronics [18–20]. Within the realm of piezotronics, the piezoelectric coupling responses in extension, shear, torsion, bending and thickness stretch scenarios have been systematically analyzed [21–28]. Hence, a specific piezoelectric potential barrier in the PSs can be achieved by the target deformations.

Nevertheless, the operating environment of PS devices is invariably subject to temperature variations. Factors including pyroelectric, thermo-elastic and thermoelectric couplings (including Seebeck and Peltier

G. Zhang (✉) · X. Kong · C. Mi (✉)
Jiangsu Key Laboratory of Engineering Mechanics, School of Civil Engineering, Southeast University, Nanjing 210096, Jiangsu, China
e-mail: gyzhang@seu.edu.cn

C. Mi
e-mail: mi@seu.edu.cn

effects) are influenced by temperature change [29–31]. Various phenomenological theories based on continuum mechanics have been applied in investigating the thermal problems [32–41]. These thermally involved couplings and piezoelectric coupling exist simultaneously in the PSs, which results in an extraordinary coupling mechanism for energy conversion between mechanical energy, thermal energy and electric energy. Recently, Qu et al. [42] have claimed that thermal dipoles can take place in PS devices during a variety of mechanical deformations. In addition, the existence of thermal fluxes in a PS plate generated by the thermoelectric effect via the electric currents can be controlled, especially under uniform transverse loadings.

PSs with thermoelectric properties have attracted significant attention in temperature sensors, electronic cooling and thermal control [43–46]. More specifically, the solid-state PS devices have main advantages in durability, reliability and safety under extreme environments compared to the conventional fluid- or gas-state devices. To extend the above-mentioned work and enhance the safety performance of PS devices, the physical responses of PS devices under the action of in-plane mechanical loads are desirable to be investigated. To effectively generate in-plane mechanical loads, the application of friction on both sides of a plate-type's surfaces can facilitate the creation of appropriate midplane forces. Furthermore, strategically distributing magnetic materials within the body of PS devices can enable the remote manipulation of these external mechanical forces. This approach not only enhances the precision of force application but also broadens the scope of control in various technological applications.

This paper aims to establish a model framework for in-plane extensional thermo-piezoelectric semiconductor films and explore the new application about current manipulation and thermal control in PS devices. Note that very few models considered the Peltier effect in thermo-piezoelectric semiconductors and disregarded the electric currents formed by the temperature gradient due to the Seebeck effect, leading to incorrect predictions. Hence, we consider the combined thermoelectric effects (i.e., the Peltier and Seebeck effects), pyroelectric effect and thermo-elastic effect on the overall physical field distributions in the current two-dimensional boundary value problems under simultaneous mechanical loads.

In this paper, Sect. 2 briefly derives the two-dimensional governing equations for thermo-piezoelectric semiconductor films considering thermo-couplings. Section 3 demonstrates the numerical analysis of the nonlinear models considering thermal couplings by the finite element (FE) method, along with the interpretation of current manipulation and thermal control. An application simulation of the previous findings about thermal control of periodic structures is introduced in Sect. 4. The final section concludes with some observations and suggestions.

2 Two-dimensional theory for thermo-piezoelectric semiconductors

For a thermo-piezoelectric semiconductor, the time-independent field equations are composed of the stress equation of motion (Newton's law), the charge equation of electrostatics (Gauss' law) including doping and mobile charges, the conservation of charge for holes and electrons (continuity equations), and the heat conduction equation [42, 47–50]:

$$\begin{aligned} &T_{ij,j} + f_i = 0, \\ &D_{i,i} = q(p - n + N_D^+ - N_A^-), \\ &J_{i,i}^p = 0, \\ &J_{i,i}^n = 0, \\ &q_{i,i} = (J_i^p + J_i^n)E_i, \end{aligned} \tag{1}$$

where T_{ij} represents the stress tensor; f_i is the body force; D_i denotes the electric displacement; q is the elementary charge; p and n are the concentrations of holes and electrons; $N_D{}^+$ and $N_A{}^-$ are the concentrations of ionized donors and acceptors; J_i^p and J_i^n represent the current densities for holes and electrons; q_i denotes the heat flux density; and E_i is the electric field.

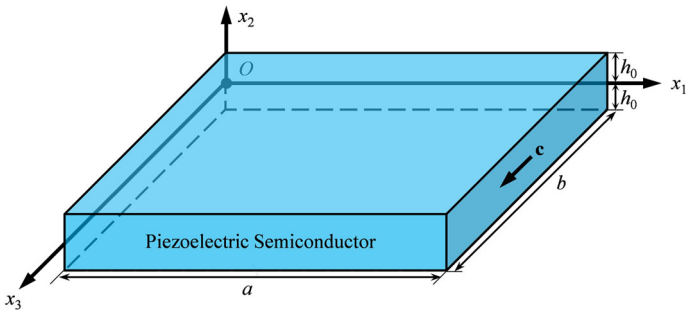

Fig. 1 A piezoelectric semiconductor thin film with an in-plane c-axis and coordinate system

Let θ be the small temperature change between the current temperature θ_{A} and the reference temperature θ_{R}, with$\theta = \theta_{\mathrm{A}} - \theta_{\mathrm{R}}$. The constitutive equations can be expressed as [42, 49, 51]

$$\begin{aligned} T_{ij} &= c_{ijkl}S_{kl} - e_{kij}E_k - \lambda_{ij}\theta, \\ D_i &= e_{ijk}S_{jk} + \varepsilon_{ij}E_j + p_i\theta, \\ J_i^p &= qp\mu_{ij}^p(E_j - \alpha_{jk}^p\theta_{,k}) - qD_{ij}^p p_{,j}, \\ J_i^n &= qn\mu_{ij}^n(E_j - \alpha_{jk}^n\theta_{,k}) + qD_{ij}^n n_{,j}, \\ q_i &= -k_{ij}\theta_{,j} + (P_{ij}^p J_j^p + P_{ij}^n J_j^n), \end{aligned} \tag{2}$$

where c_{ijkl} denotes the elastic tensor; S_{kl} is the strain tensor; e_{kij} is the piezoelectric tensor; λ_{ij} is the thermo-elastic tensor; ε_{ij} is the dielectric tensor; p_i is the pyroelectric tensor; μ_{ij}^p and μ_{ij}^n denote the carrier mobility; α_{jk}^p and α_{jk}^n represent the Seebeck coefficients; P_{ij}^p and P_{ij}^n are the Peltier coefficients; D_{ij}^p and D_{ij}^n represent the carrier diffusion constants; and k_{ij} represents the thermal conductivity.

The gradient relations read,

$$S_{ij} = (u_{i,j} + u_{j,i})/2, \quad E_i = -\varphi_{,i}, \tag{3}$$

where u_i is the mechanical displacement and φ is the potential for electrostatics.

It is noted that, for thermo-piezoelectric semiconductors used in microelectronic devices, the temperature changes are minimal. Thereby, we have the following relations under the small temperature perturbation assumption (i.e., $\theta << \theta_{\mathrm{R}}$) [29, 51]:

$$\frac{P_{11}^n}{\alpha_{11}^n} = \frac{P_{11}^p}{\alpha_{11}^p} = \theta_{\mathrm{A}} \simeq \theta_{\mathrm{R}}, \quad \frac{D_{11}^n}{\mu_{11}^n} = \frac{D_{11}^p}{\mu_{11}^p} = \frac{k_{\mathrm{B}}\theta_{\mathrm{A}}}{q} \simeq \frac{k_{\mathrm{B}}\theta_{\mathrm{R}}}{q}, \tag{4}$$

where$k_{\mathrm{B}} = 1.3806 \times 10^{-23}$ J K^{-1} is the Boltzmann constant.

As shown in Fig. 1, for a thermo-piezoelectric semiconductor of crystals in the 6mm point group (e.g., ZnO), the c-axis is parallel to the x_3-direction. The in-plane electromechanical loads are considered in this model, thus, the zero-order field equations describing the extension deformations are needed [49]:

$$\begin{aligned} &u_1 = u(x_1, x_3), \quad u_3 = v(x_1, x_3), \quad \varphi = \varphi(x_1, x_3), \\ &\theta = \theta(x_1, x_3), \quad p = p(x_1, x_3), \quad n = n(x_1, x_3). \end{aligned} \tag{5}$$

Let the thickness of the film be $2h_0$. Assume that the semiconductor film is subjected to n-type doping, and ignore the effects of p-type doping (i.e., $p = 0$). Consider stress relaxation $T_{22} = 0$ for plane stress problems. The constitutive equations for the film can be expressed as:

$$\begin{aligned}
T_{11} &= \overline{c}_{11}S_{11} + \overline{c}_{13}S_{33} - \overline{e}_{31}E_3 - \overline{\lambda}_{11}\theta,\\
T_{33} &= \overline{c}_{13}S_{11} + \overline{c}_{33}S_{33} - \overline{e}_{33}E_3 - \overline{\lambda}_{33}\theta,\\
T_{13} &= 2\overline{c}_{44}S_{13} - \overline{e}_{15}E_1,\\
D_1 &= \overline{\varepsilon}_{11}E_1 + 2\overline{e}_{15}S_{13},\\
D_3 &= \overline{\varepsilon}_{33}E_3 + \overline{e}_{31}S_{11} + \overline{e}_{33}S_{33} + \overline{p}_3\theta,\\
J_1^n &= qn\mu_{11}^n(E_1 - \alpha_{11}^n\theta_{,1}) + qD_{11}^n n_{,1},\\
J_3^n &= qn\mu_{33}^n(E_3 - \alpha_{33}^n\theta_{,3}) + qD_{33}^n n_{,3},\\
q_1 &= -k_{11}\theta_{,1} + qP_{11}^n(n\mu_{11}^n(E_1 - \alpha_{11}^n\theta_{,1}) + D_{11}^n n_{,1}),\\
q_3 &= -k_{33}\theta_{,3} + qP_{33}^n(n\mu_{33}^n(E_3 - \alpha_{33}^n\theta_{,3}) + D_{33}^n n_{,3}),
\end{aligned} \tag{6}$$

where

$$\begin{aligned}
&\overline{c}_{11} = c_{11} - \frac{c_{12}^2}{c_{11}}, \quad \overline{c}_{13} = c_{13} - \frac{c_{12}c_{13}}{c_{11}}, \quad \overline{c}_{33} = c_{33} - \frac{c_{13}^2}{c_{11}}, \quad \overline{c}_{44} = c_{44},\\
&\overline{\lambda}_{11} = \lambda_{11} - \frac{c_{12}}{c_{11}}\lambda_{11}, \quad \overline{\lambda}_{33} = \lambda_{33} - \frac{c_{13}}{c_{11}}\lambda_{11}, \quad \overline{e}_{15} = e_{15}, \quad \overline{e}_{31} = e_{31} - \frac{c_{12}}{c_{11}}e_{31},\\
&\overline{e}_{33} = e_{33} - \frac{c_{13}}{c_{11}}e_{31}, \quad \overline{\varepsilon}_{11} = \varepsilon_{11}, \quad \overline{\varepsilon}_{33} = \varepsilon_{33} + \frac{e_{31}^2}{c_{11}}, \quad \overline{p}_3 = p_3 + \frac{e_{31}}{c_{11}}\lambda_{11}.
\end{aligned} \tag{7}$$

Substituting the field equations in Eq. (5) and constitutive equations in Eq. (6) into Eq. (1), and integrating the equations along the thickness direction (i.e., x_2-direction), we got the 2-D governing equations:

$$\begin{aligned}
&\mathcal{N}_{11,1} + \mathcal{N}_{31,3} + \mathcal{F}_1 = 0,\\
&\mathcal{N}_{13,1} + \mathcal{N}_{33,3} + \mathcal{F}_3 = 0,\\
&\mathcal{D}_{1,1} + \mathcal{D}_{3,3} + \mathcal{D} = 2qh_0(-n + N_D^+),\\
&\mathcal{J}_{1,1}^n + \mathcal{J}_{3,3}^n + \mathcal{J} = 0,\\
&\mathcal{Q}_{1,1} + \mathcal{Q}_{3,3} + \mathcal{Q} = \mathcal{J}_1^n E_1 + \mathcal{J}_3^n E_3,
\end{aligned} \tag{8}$$

where the film forces for the extensional motion, the electric displacement resultants, the current resultants and the thermal flux resultants are defined by the following integral along the film thickness:

$$[\mathcal{N}_{ij},\ \mathcal{D}_i,\ \mathcal{J}_i^n,\ \mathcal{Q}_i] = \int_{-h_0}^{h_0} [T_{ij},\ D_i,\ J_i^n,\ q_i]\, dx_2, \quad i, j = 1, 3. \tag{9}$$

In Eq. (8), the contributions from the internal body force loads, the surface electromechanical loads and the surface heat fluxes on the top and bottom of the film are represented by

$$\begin{aligned}
&\mathcal{F}_i = T_{2i}(h_0) - T_{2i}(-h_0) + \int_{-h_0}^{h_0} f_i dx_2, \quad \mathcal{D} = D_2(h_0) - D_2(-h_0),\\
&\mathcal{J} = J_2^n(h_0) - J_2^n(-h_0), \quad \mathcal{Q} = q_2(h_0) - q_2(-h_0).
\end{aligned} \tag{10}$$

We denote $n_0 = N_D^+$, a constant for uniform doping and write$n = n_0 + \Delta n$. In addition, the contributions of electrical and thermal surface loads in Eq. (10) are ignored. Substituting Eqs. (3), (6) and (9) into Eq. (8), we obtain five governing equations for u, v, φ, θ and n:

$$\begin{aligned}
&\overline{c}_{11}u_{,11} + \overline{c}_{13}v_{,31} + \overline{e}_{31}\varphi_{,31} - \overline{\lambda}_{11}\theta_{,1} + \overline{c}_{44}(u_{,33} + v_{,13}) + \overline{e}_{15}\varphi_{,13} + \frac{\mathcal{F}_1}{2h_0} = 0,\\
&\overline{c}_{44}(u_{,31} + v_{,11}) + \overline{e}_{15}\varphi_{,11} + \overline{c}_{13}u_{,13} + \overline{c}_{33}v_{,33} + \overline{e}_{33}\varphi_{,33} - \overline{\lambda}_{33}\theta_{,3} + \frac{\mathcal{F}_3}{2h_0} = 0,\\
&\overline{e}_{15}(u_{,31} + v_{,11}) - \overline{\varepsilon}_{11}\varphi_{,11} + \overline{e}_{31}u_{,13} + \overline{e}_{33}v_{,33} - \overline{\varepsilon}_{33}\varphi_{,33} + \overline{p}_3\theta_{,3} = q\Delta n,\\
&q[D_{11}^n n_{,1} - n\mu_{11}^n(\varphi_{,1} + \alpha_{11}^n\theta_{,1})]_{,1} + q[D_{33}^n n_{,3} - n\mu_{33}^n(\varphi_{,3} + \alpha_{33}^n\theta_{,3})]_{,3} = 0,\\
&-k_{11}\theta_{,11} - k_{33}\theta_{,33} + qP_{11}^n[D_{11}^n n_{,1} - n\mu_{11}^n(\varphi_{,1} + \alpha_{11}^n\theta_{,1})]_{,1} + qP_{33}^n[D_{33}^n n_{,3} - n\mu_{33}^n(\varphi_{,3} + \alpha_{33}^n\theta_{,3})]_{,3}\\
&= -q\varphi_{,1}[D_{11}^n n_{,1} - n\mu_{11}^n(\varphi_{,1} + \alpha_{11}^n\theta_{,1})] - q\varphi_{,3}[D_{33}^n n_{,3} - n\mu_{33}^n(\varphi_{,3} + \alpha_{33}^n\theta_{,3})].
\end{aligned} \tag{11}$$

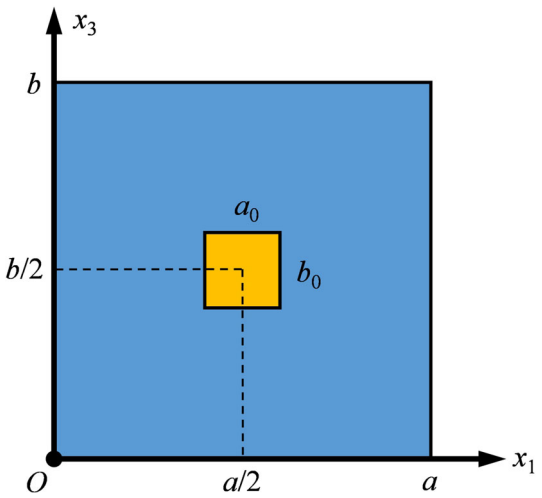

Fig. 2 Planar model under in-plane mechanical loads and the loading area

The following boundary conditions can be prescribed at the lateral boundaries of the film [42]:

$$\begin{aligned} &u = \overline{u} \quad \text{or} \quad T_{NN} = \overline{t}_N, \quad v = \overline{v} \quad \text{or} \quad T_{NS} = \overline{t}_S, \\ &D_N = \overline{D}_N \quad \text{or} \quad \varphi = \overline{\varphi}, \quad J_N = \overline{J}_N \quad \text{or} \quad n = \overline{n}, \\ &q_N = \overline{q}_N \quad \text{or} \quad \theta = \overline{\theta}. \end{aligned} \tag{12}$$

3 Numerical results and discussion

In this section, we solved the nonlinear governing equations given in Eq. (11). When the thermal couplings are considered, the flow of electric currents gives rise to the Joule heating effect. Concurrently, the Peltier effect induces heat fluxes to converge at the boundaries and flow through the structure, thereby affecting the temperature field. Moreover, temperature change is incorporated into the iterative calculation of both stress and polarization, making the acquisition of an analytical solution challenging. Therefore, we employ COMSOL® Multiphysics for FE analysis to perform numerical results.

In our research, we employed the two-dimensional partial differential equation (PDE) module for conducting nonlinear analysis. Equation (11) was input into this PDE module, and the simulation results were then obtained by processing this equation with the predefined boundary conditions. For our analysis, we opted for a steady-state approach. We utilized the automatic Newton method for solving the nonlinear equations and setting the convergence criterion such that the process terminates when the tolerance level falls below 0.001. This approach ensured that we achieved accurate and reliable results from our simulations.

To validate the accuracy of FE analysis, a comparison between analytical results and FE results is made in Appendix A. Notably, both results are obtained from the linearized governing equations, and to a certain extent, the accuracy can be validated.

Our objective in solving the defined boundary value problem is to investigate the impact of mechanically induced potential on electric currents and thermal fluxes. This holds potential utility for applications involving thermal control in PS devices.

This research focuses on an n-type doped ZnO semiconductor thin film that is subjected to in-plane static extensional deformations. Consider a planar model under in-plane mechanical loads as shown in Fig. 2. Size of the film is $a \times b$, and the size of the mechanical loading area, which is located in the center of the film, is$a_0 \times b_0$. The thickness of the film is $2h_0$, and all four edges are fixed mechanically. Geometric parameters in this section are: $a = b = 1\mu\text{m}$, $a_0 = b_0 = 0.2\mu\text{m}$ and $2h_0 = 20\text{nm}$. The material parameters employed in the numerical examples are given in Table 1 (under the reference temperature $\theta_\text{R} = 300$ K) [42, 49, 51, 52].

Table 1 Material parameters of *n*-type ZnO

Physical quantities	Symbol	Value
Elastic constants (GPa)	c_{11}, c_{33}, c_{12}, c_{13}, c_{44}, c_{66}	209.7, 210.9, 121.1, 105.1, 42.47, 44.3
Piezoelectric constants (C m^{-2})	e_{15}, e_{31}, e_{33}	− 0.48, − 0.573, 1.32
Dielectric constants (C m^{-1} V^{-1})	ε_{11}, ε_{33}	7.57×10^{-11}, 9.027×10^{-11}
Thermo-elastic constants (N m^{-2} K^{-1})	λ_{11}, λ_{33}	6.132×10^{5}, 10.0225×10^{5}
Mobility (m^2 V^{-1} s^{-1})	μ_{11}^{n}, μ_{33}^{n}	0.02, 0.02
Diffusion constants (m^2 s^{-1})	D_{11}^{n}, D_{33}^{n}	5.177×10^{-4}, 5.177×10^{-4}
Thermal conductivity (W m^{-1} K^{-1})	k_{11}, k_{33}	15,15
Pyroelectric constants (C m^{-2} K^{-1})	p_1, p_3	-9.3×10^{-6}, -9.3×10^{-6}
Doping level (m^{-3})	N_D^+	10^{21}
Seebeck coefficients (V K^{-1})	α_{11}^{n}, α_{33}^{n}	-180×10^{-6}, -180×10^{-6}
Peltier coefficients (V)	P_{11}^{n}, P_{33}^{n}	− 0.054, − 0.054

Based on the requirement of linear constitutive, the deformation of the material is limited at the elastic level. In our methodology, the effective von Mises strain S_{eff} is used as a reference for strain level analysis [53]:

$$S_{\text{eff}} = \sqrt{\frac{2}{3}(S_{11}^2 + S_{33}^2 + 2S_{13}^2)}. \tag{13}$$

Note that the zero items have been ignored in S_{eff}. We limit the equivalent von Mises strain S_{eff} to less than or equal to 0.01% to ensure that the material is in the elastic deformation stage (i.e., $S_{\text{eff}} \leq 0.01\%$).

Furthermore, because the piezoelectric coefficients are considered constants in our analysis, the strain magnitude is one of the key determinants of the piezoelectric potential of the structure. We have observed that when the piezoelectric potential is close in magnitude to the external voltage, the piezoelectric effect becomes more pronounced. Meanwhile, the doping level influences the currents in the structure. Therefore, in our study, the given external voltage and doping level are the determinants in determining the magnitude of force that can produce a noticeable piezoelectric effect.

3.1 Current manipulation switches

Assuming that the temperature variations at $x_3 = 0$ and b are zero, and the thermal fluxes vanish at$x_1 = 0$ and a (i.e., adiabatic). The voltage $\overline{\varphi}$ is applied at$x_3 = b$ with $\overline{\varphi} = 0.05$V. Ohm contacts are used at$x_3 = 0$ and b so that no charge accumulations are formed, and$x_1 = 0$ and a are electrically open. A uniform mechanical load $\mathcal{F}_3$ is applied at the loading area, with the magnitude t_3 ranges from -3×10^6 N m^{-2} to 3×10^6 N m^{-2}. That is, for the planar model in Fig. 2, the boundary conditions are:

$$\begin{aligned}
&u = 0, \quad v = 0, \quad J_1 = 0, \quad D_1 = 0, \quad q_1 = 0 \quad \text{at} \quad x_1 = 0,\ a,\\
&u = 0, \quad v = 0, \quad \varphi = 0, \quad \Delta n = 0, \quad \theta = 0 \quad \text{at} \quad x_3 = 0,\\
&u = 0, \quad v = 0, \quad \varphi = \overline{\varphi}, \quad \Delta n = 0, \quad \theta = 0 \quad \text{at} \quad x_3 = b,\\
&\begin{cases}
\mathcal{F}_1 = 0, & \text{all},\\
\mathcal{F}_3 = t_3, \quad in \quad \dfrac{a - a_0}{2} < x_1 < \dfrac{a + a_0}{2} \quad \text{and} \quad \dfrac{b - b_0}{2} < x_3 < \dfrac{b + b_0}{2}, & \\
\mathcal{F}_3 = 0, & \text{elsewhere}.
\end{cases}
\end{aligned} \tag{14}$$

Figures 3 and 4 show the field distributions within the *n*-type ZnO film induced by uniform mechanical loads $t_3 = \pm 2 \times 10^6$ N m^{-2}, respectively. As depicted in Figs. 3a and 4a, observations indicate that the forces applied generate electrostatic potential barriers through the piezoelectric coupling. In Figs. 3c and 4c, the electrons are attracted to regions with high potential, driven by the electric field, and form electric currents in the plane. It can be seen that the current density is indeed symmetrical about both the centerlines $x_1 = a/2$ and $x_3 = b/2$.

Figures 3b and 4b display the distributions of temperature change, which are significantly influenced by the variation in currents. Figures 3d and 4d show the synthesis process of thermal fluxes under the influence

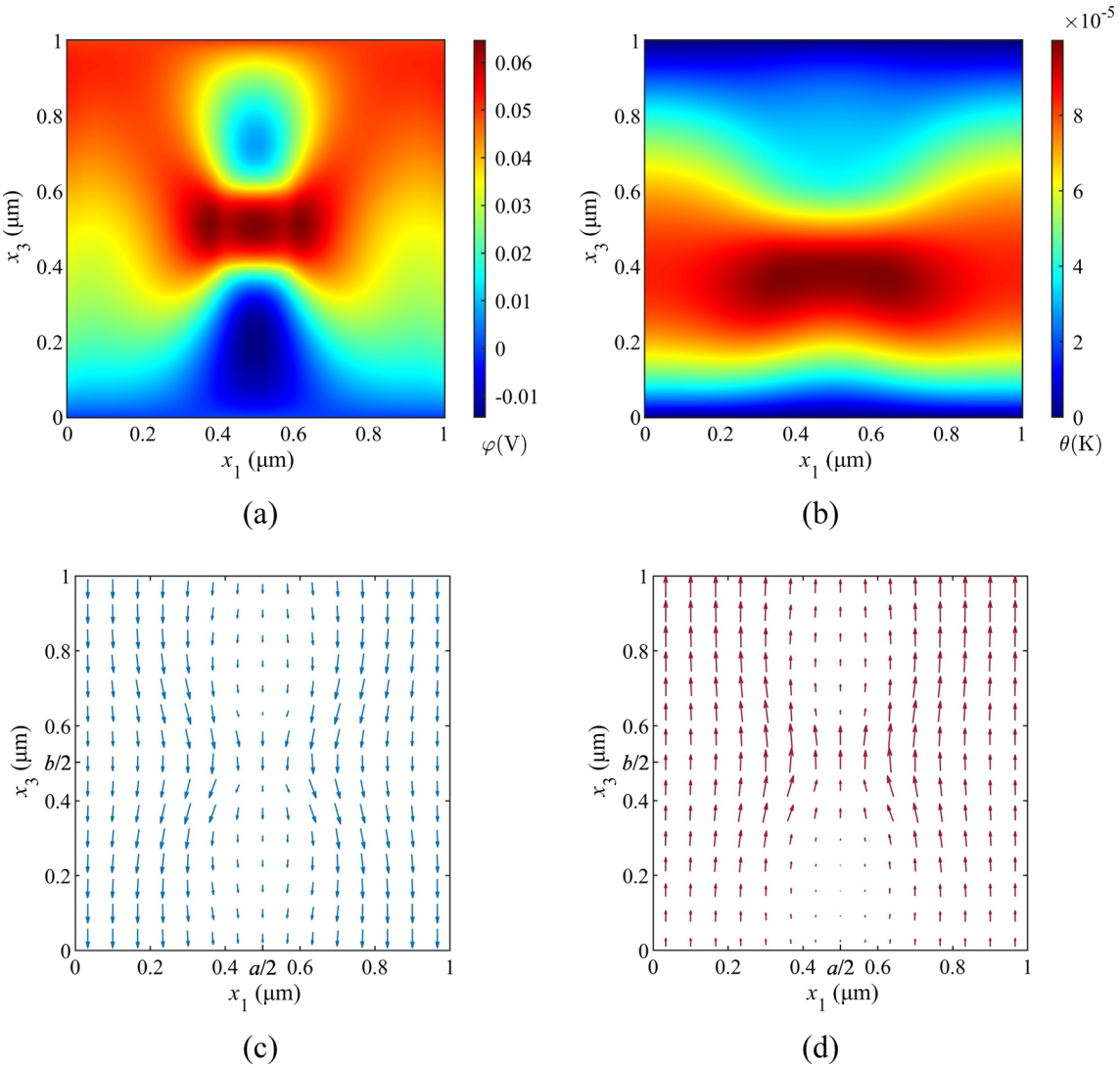

Fig. 3 Field distributions in the *n*-type ZnO film induced by a uniform mechanical load $t_3 = 2 \times 10^6$ N m^{-2}: **a** electrostatic potential, **b** temperature field, **c** electric current density and **d** thermal flux density

of the Peltier effect. It should be noted that the thermal fluxes are the sum of the Peltier effect-induced fluxes and the heat conduction fluxes. Given that the temperature fields are not symmetric about the centerline $x_3 = b/2$, the thermal density is only symmetric about the centerline $x_1 = a/2$.

However, given that the defined boundary conditions restrict the temperature change on the boundary in the x_3-direction, the heat fluxes resulting from the Peltier effect are ultimately flowing out of the boundaries, thereby not influencing the temperature field in this instance.

Comparing the temperature fields in Figs. 3b and 4b, it can be seen that the temperature change is more intense when the force points to the positive x_3-direction. In order to explore the reason of this phenomenon, we define the magnitude of the total average current I_3^{Tot} through the boundaries in the x_3-direction, as

$$I_3^{\mathrm{Tot}} = h_0 \int_0^a J_3|_{x_3=0} \mathrm{d}x_1 + h_0 \int_0^a J_3|_{x_3=b} \mathrm{d}x_1. \tag{15}$$

As depicted in Fig. 5, the magnitude of the total average current fluctuates in response to changes in mechanical force. When a force is applied pointing to the positive x_3-direction (i.e., the c-axis direction) to the structure, there is an increase in the total current, whereas the application of a force in the opposite direction suppresses the total current. At the max strain level of 0.01% (i.e., $S_{\max\ \mathrm{eff}} = 1 \times 10^{-4}$, approximately t_3

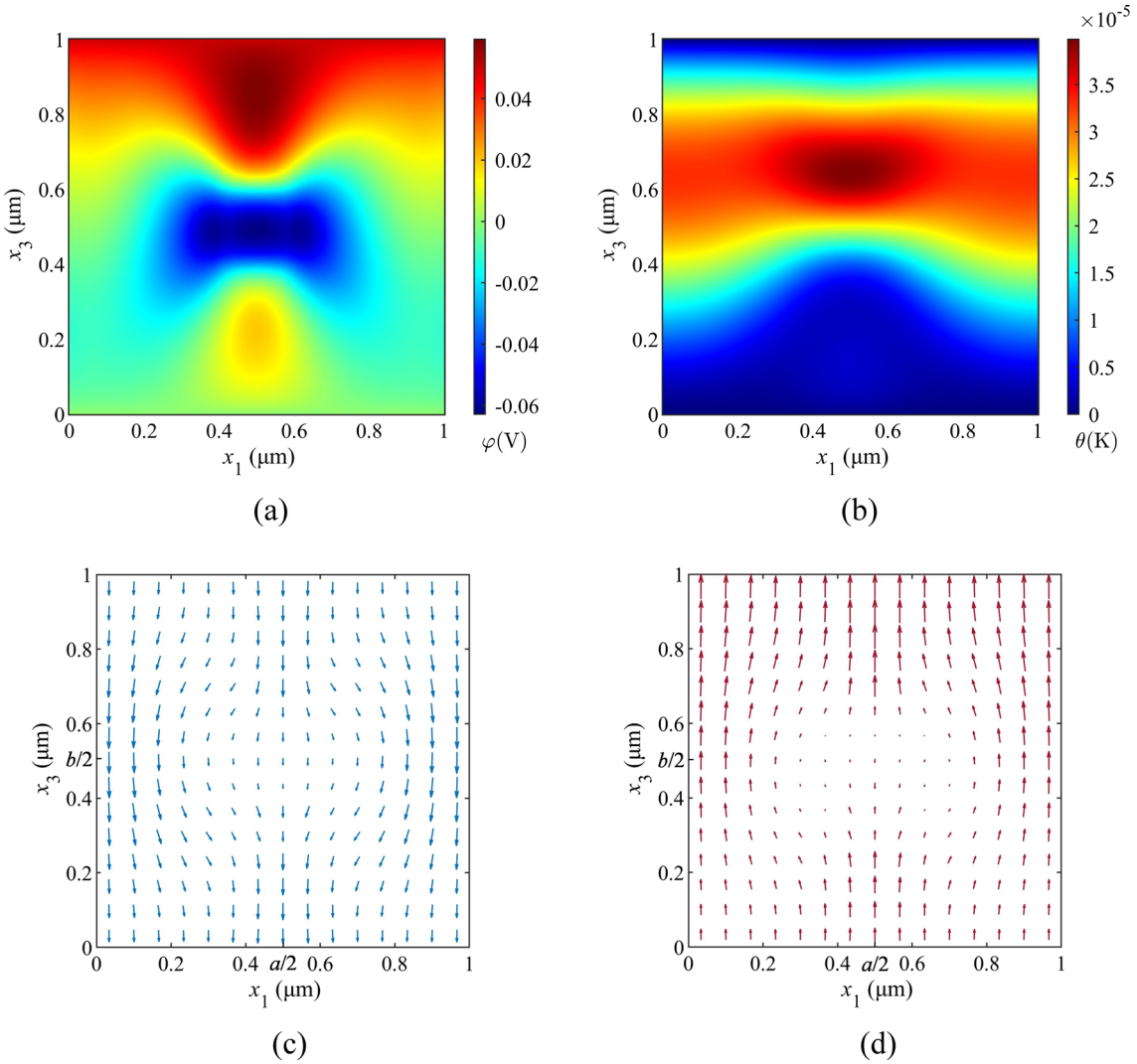

Fig. 4 Field distributions in the *n*-type ZnO film induced by a uniform mechanical load $t_3 = -2 \times 10^6$ N m^{-2}: **a** electrostatic potential, **b** temperature field, **c** electric current density and **d** thermal flux density

$= -2.2 \times 10^6$ N m^{-2}), the magnitude of electric current can be reduced by 70.4% in comparison with its counterpart in the absence of an external force. Such a PS device under mechanical loadings provides a design for electronic components that need current switches, such as sensors.

As previously mentioned, the thermal fluxes resulting from the Peltier effect contribute rarely to the temperature field in this case. When the boundary conditions change, the thermoelectric effect will significantly affect the temperature field of the structure, an instance that will be discussed in Sect. 3.2.

3.2 Influence of Peltier effect on temperature field

To investigate the impact of the Peltier effect on the temperature field of the structure, we interchange the thermal boundary conditions at the boundaries of x_1- and x_3-directions. It is assumed that the temperature changes at$x_1 = 0$ and a are zero, while $x_3 = 0$ and b are adiabatic. The other boundary conditions remain the same as in Sect. 3.1. The boundary conditions are changed as

$$u = 0, \quad v = 0, \quad J_1 = 0, \quad D_1 = 0, \quad \theta = 0 \quad \text{at} \quad x_1 = 0,\ a,$$
$$u = 0, \quad v = 0, \quad \varphi = 0, \quad \Delta n = 0, \quad q_3 = 0 \quad \text{at} \quad x_3 = 0,$$

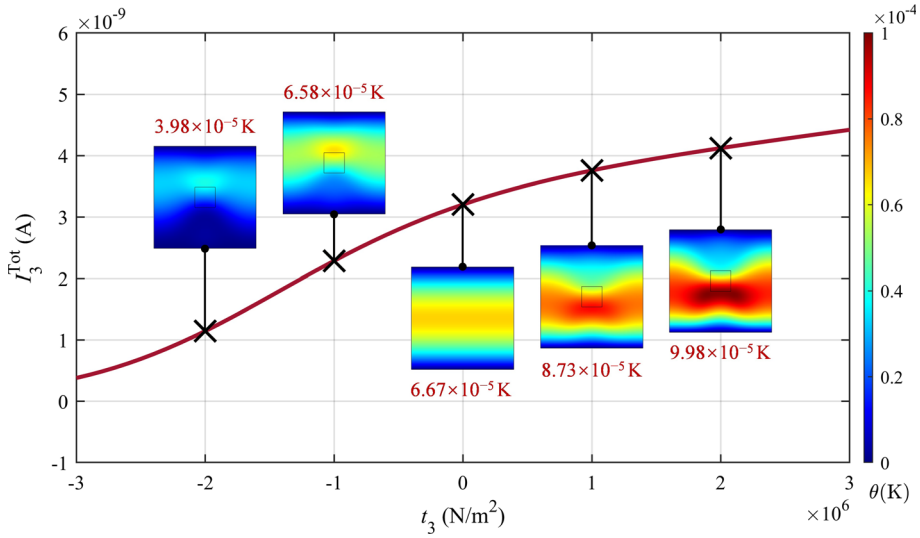

Fig. 5 Magnitude of total average current through the boundary in the x_3-direction and temperature perturbation under different uniform mechanical loads

$$u = 0, \quad v = 0, \quad \varphi = \overline{\varphi}, \quad \Delta n = 0, \quad q_3 = 0 \quad \text{at} \quad x_3 = b,$$
$$\begin{cases} \mathcal{F}_1 = 0, & \text{all}, \\ \mathcal{F}_3 = t_3, \quad in \quad \dfrac{a-a_0}{2} < x_1 < \dfrac{a+a_0}{2} \quad \text{and} \quad \dfrac{b-b_0}{2} < x_3 < \dfrac{b+b_0}{2}, \\ \mathcal{F}_3 = 0, & \text{elsewhere}. \end{cases} \tag{16}$$

Figure 6 presents a comparison of the temperature fields and thermal flux distributions (indicated by the arrow) under identical boundary conditions when the uniform mechanical force $t_3 = 2 \times 10^6$ N m^{-2}, both with and without considering the Peltier effect. In a steady state, thermal fluxes are generated by the electric currents due to the Peltier effect in the direction opposite to the currents, until the Peltier effect-induced fluxes reach equilibrium with the heat conduction fluxes caused by the temperature gradient in the x_3-direction. Finally, the heat fluxes flow to the boundaries, which maintain a constant temperature (i.e.,$x_1 = 0$ and a). This results in a significant difference in temperature fields between Fig. 6a and b. Owing to the influence of Joule heat, the distribution of the temperature field is not completely symmetrical in Fig. 6a. This underscores the substantial influence of the Peltier effect on thermo-piezoelectric semiconductors.

To further demonstrate the influence of the Peltier effect, Fig. 7a displays the maximum and minimum temperature variation (i.e., $\theta_{\max}$ and $\theta_{\min}$) of the structure as the uniform mechanical loads change. When considering Peltier effect, the temperature change reaches a maximum value of 2.71×10^{-4} K at $t_3 = 7 \times 10^5$ N m^{-2} and a minimum value of -1.29×10^{-4} K at $t_3 = 0$. Figure 7b shows the max temperature range $\Delta\theta$ of the film under varying mechanical loads (i.e., $\Delta\theta = \theta_{\max} - \theta_{\min}$). The maximum value is achieved at $t_3 = 6 \times 10^5$ N m^{-2}, reaching 3.95×10^{-4} K, while its counterpart is merely 0.86×10^{-4} K. When taking the Peltier effect into account, the maximum temperature difference due to heat accumulation can escalate to a 4.6-fold increase in comparison with the scenario that neglects the Peltier effect.

Modifications in the thermal boundary predominantly impact the temperature field of the structure, whereas the temperature change induced by the Peltier effect and the Joule heating effect exerts a minimal influence on the electrostatic potential field and current density of the structure. The distributions of electrostatic potential and current density acquired are nearly identical to those in Fig. 3a and c. When we attempt to introduce an external temperature load, the substantial temperature difference influences the potential field of the structure via the Seebeck effect, thereby impacting the magnitude and direction of the structure's currents. This phenomenon has been extensively studied and discussed by many scholars [54–56].

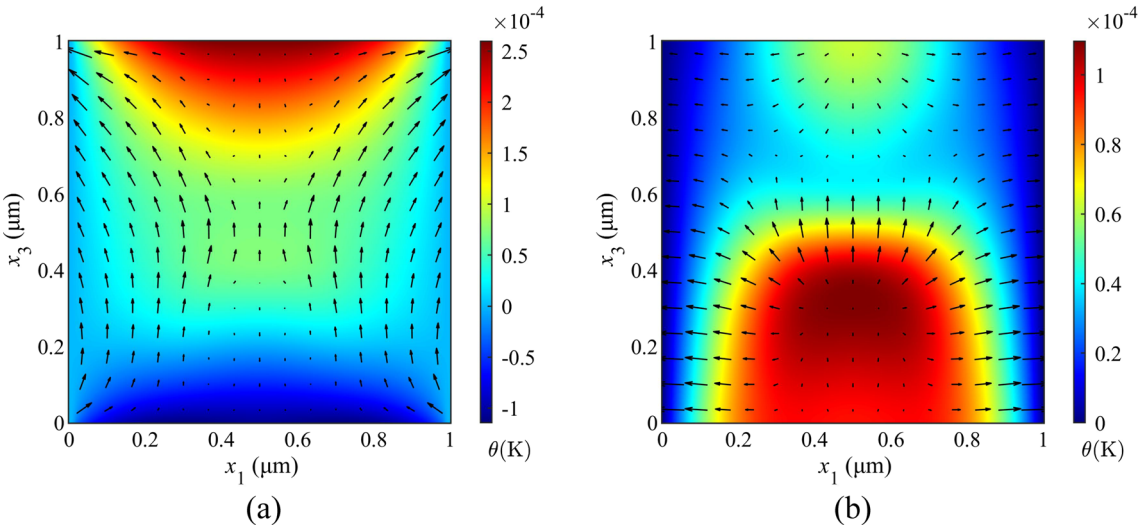

Fig. 6 Influence of the Peltier effect on the distribution of temperature field and thermal flux, **a** with Peltier effect and **b** without Peltier effect

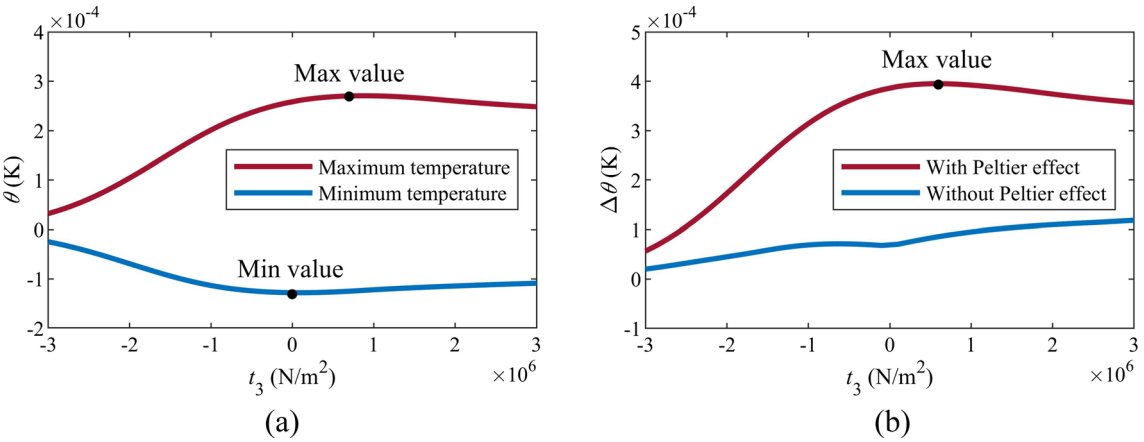

Fig. 7 Temperature variation under different uniform mechanical loads, **a** maximum and minimum temperatures, **b** influence of Peltier effect on maximum temperature range

3.3 Thermal control in PS device

In this section, a voltage $\overline{\varphi}$ is applied at$x_1 = a$, with $\overline{\varphi} = 0.05$V. The edge boundaries $x_3 = 0, b$ are electrically open. The mechanical loads in both the x_1- and x_3-directions are considered. Thermally, $x_3 = 0, b$ are adiabatic, and $x_1 = 0$, a maintain a constant temperature. The boundary conditions have the following forms:

$$
\begin{aligned}
&u = 0, \quad v = 0, \quad \varphi = 0, \quad \Delta n = 0, \quad \theta = 0 \quad \text{at} \quad x_1 = 0,\\
&u = 0, \quad v = 0, \quad \varphi = \overline{\varphi}, \quad \Delta n = 0, \quad \theta = 0 \quad \text{at} \quad x_1 = a,\\
&u = 0, \quad v = 0, \quad J_3 = 0, \quad D_3 = 0, \quad q_3 = 0 \quad \text{at} \quad x_3 = 0,\ b,\\
&\begin{cases}
\mathcal{F}_1 = 0, & \text{all},\\
\mathcal{F}_3 = t_3, \quad in \quad \dfrac{a - a_0}{2} < x_1 < \dfrac{a + a_0}{2} \quad \text{and} \quad \dfrac{b - b_0}{2} < x_3 < \dfrac{b + b_0}{2}, & \\
\mathcal{F}_3 = 0, & \text{elsewhere}.
\end{cases}
\end{aligned}
$$

or

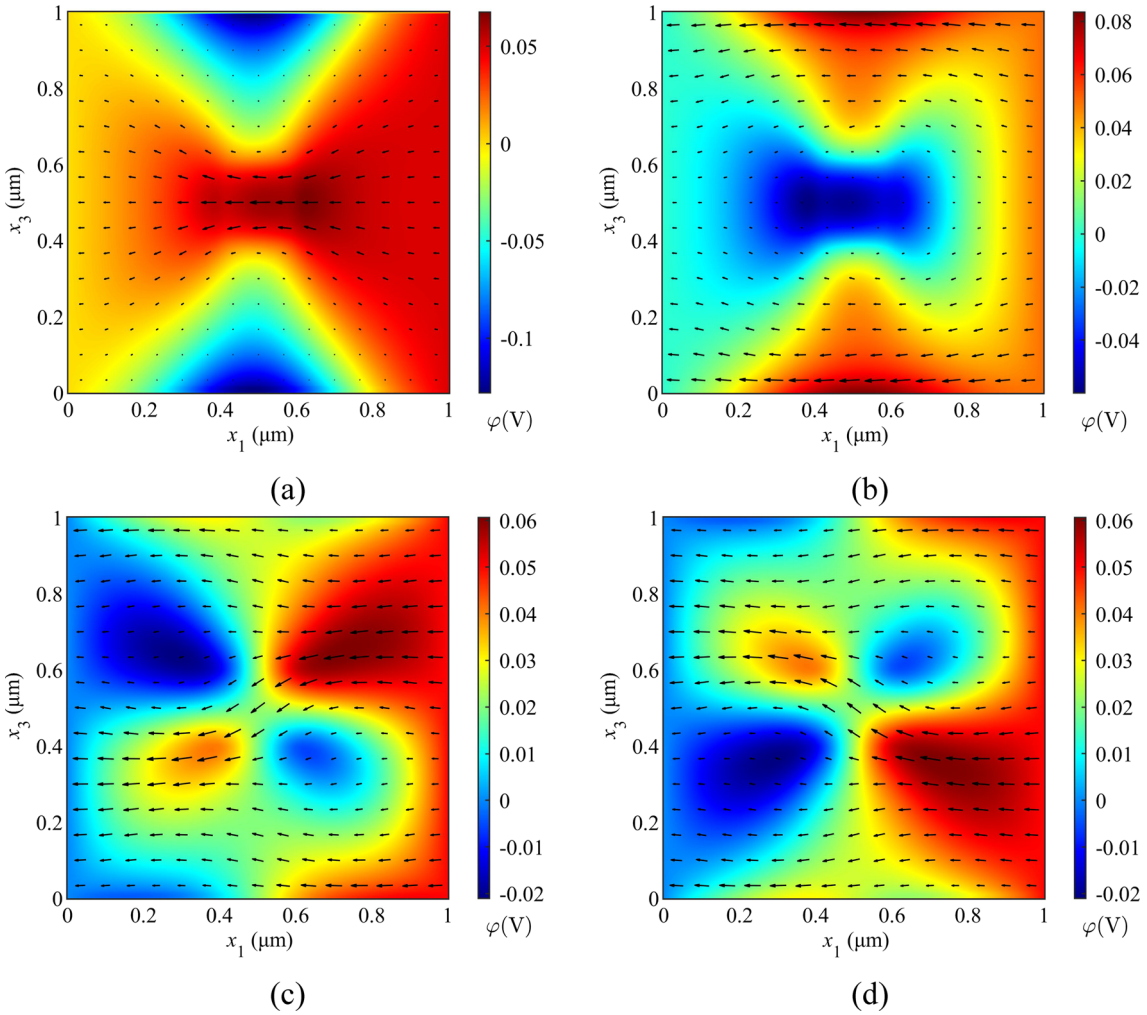

Fig. 8 Distributions of electrostatic potential and current density due to uniform mechanical loads: **a** $t_3 = 2 \times 10^6$ N m^{-2}, $t_1 = 0$, **b** $t_3 = -2 \times 10^6$ N m^{-2}, $t_1 = 0$, **c** $t_1 = 2 \times 10^6$ N m^{-2}, $t_3 = 0$ and **d** $t_1 = -2 \times 10^6$ N m^{-2}, $t_3 = 0$

$$\begin{cases} \mathcal{F}_3 = 0, & \text{all}, \\ \mathcal{F}_1 = t_1, & in \quad \dfrac{a-a_0}{2} < x_1 < \dfrac{a+a_0}{2} \quad \text{and} \quad \dfrac{b-b_0}{2} < x_3 < \dfrac{b+b_0}{2}, \\ \mathcal{F}_1 = 0, & \text{elsewhere}. \end{cases} \tag{17}$$

Figure 8 shows the distributions of electrostatic potential and current density (indicated by the arrow) under different uniform mechanical loads. It can be seen that, under the action of mechanical loads, potential barriers and wells are generated within the film due to the piezoelectric coupling, as mentioned before. Electrons are attracted to areas with higher potential, while simultaneously bypassing areas with lower potential, thereby generating corresponding currents. Mechanical loads in both the x_1- and x_3-directions significantly affect the temperature distribution of the structure. The force directed toward the positive x_3-direction generates a potential barrier at the center part of the film, as shown in Fig. 8a. Thereby, the currents accumulate at the potential barrier and heat up, leading to a temperature rise. Figure 9 depicts the distributions of temperature field and heat flux (also indicated by the arrow) under different mechanical loads. As depicted in Fig. 9a, the magnitude of temperature is increased by 1.4 times compared with the place where the current density is sparse on the line a-a. On the contrary, a force in the opposite direction induces a potential well (see Fig. 8b) and modulates the currents to bypass the loading area, thereby generating a temperature loss. The lowest temperature on the line a-a is only 0.39 times the highest temperature in Fig. 9b. In Fig. 8c and d, the external forces directed to the x_1-direction induce pairs of centrally symmetric electrostatic potential barriers and wells.

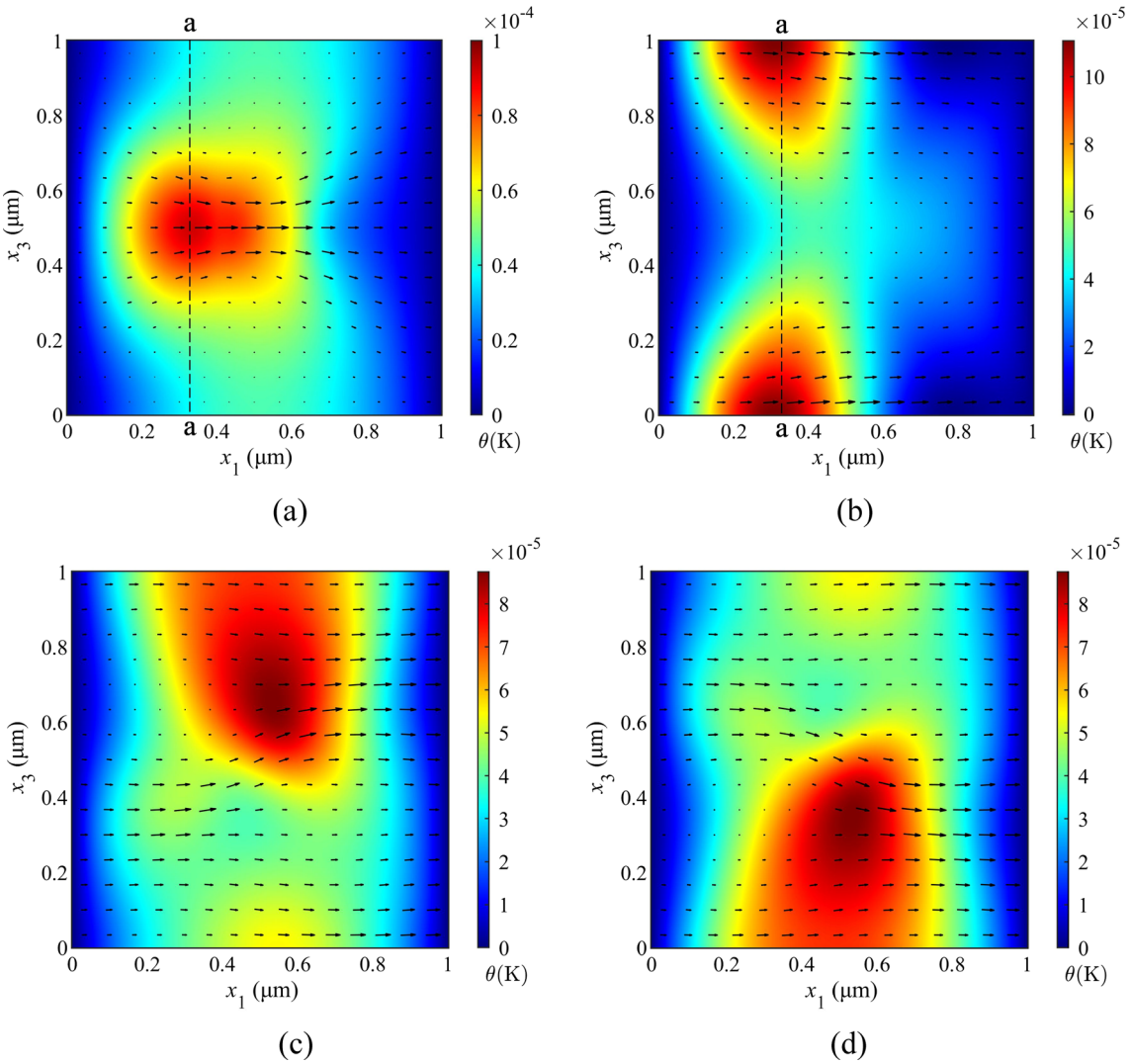

Fig. 9 Distributions of temperature field and thermal flux due to uniform mechanical loads: **a** $t_3 = 2 \times 10^6$ N m^{-2}, $t_1 = 0$, **b** $t_3 = -2 \times 10^6$ N m^{-2}, $t_1 = 0$, **c** $t_1 = 2 \times 10^6$ N m^{-2}, $t_3 = 0$ and **d** $t_1 = -2 \times 10^6$ N m^{-2}, $t_3 = 0$

In the presence of an applied voltage, the potential difference in certain regions becomes more pronounced. Consequently, the currents follow the path of high potential, leading to a more effective heating effect in some regions, as shown in Fig. 9c and d.

It should be noted that the results indicate that the field distributions show the characteristics of linear superposition. The resultant force in any direction can be decomposed into forces pointing to the x_1- and x_3-directions, and the field distributions are linearly superimposed. In addition, when the direction of the current is perpendicular to the poling direction of the material, the intervention of the external force primarily acts on redirecting the local electric current rather than its magnitude, which is obviously different from that in Sect. 3.1. Therefore, this study proposes a potential method for mechanically controlling the temperature of the structure. These findings offer theoretical support for the potential to manipulate electric heating devices through external mechanical loadings, a topic that is discussed in the next section.

4 Application of thermal control to periodic structures

In this section, we develop a model of a micro-electric heating device for periodic structures that utilizes an *n*-type doped ZnO semiconductor substrate, as presented in Fig. 10. The uniform doping concentration (i.e.,

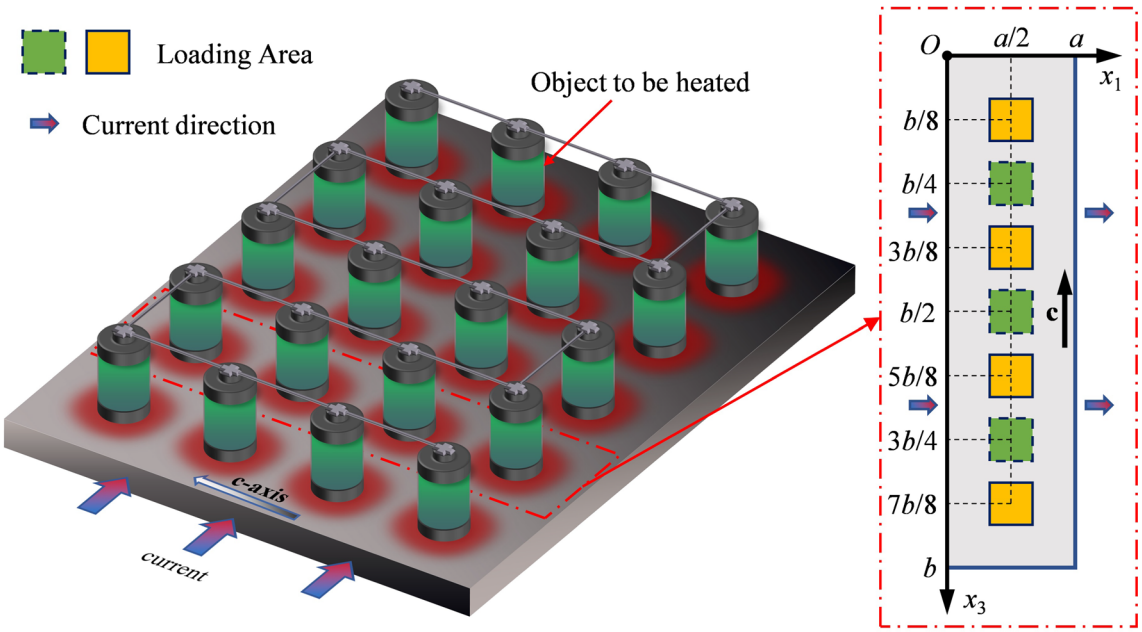

Fig. 10 Model of a micro-heating device using n-type doped ZnO-based substrate for periodic structure and the research segment

n_0) increases from 10^{21} m^{-3} to 10^{22} m^{-3}. It is assumed that the structure is sufficiently long in the x_3-direction, while its length in the x_1-direction is limited. In this context, for two lines in close proximity along the x_3-direction, we find that the temperature and potential distributions are continuous, and the temperature changes are negligible; therefore, we choose to focus on a small segment of the structure. This approach not only ensures the key assumption of small temperature perturbation, but also reduces the computational demands of FE analysis.

In Fig. 10, a square part comprising several symmetrically distributed loading areas is chosen as the subject of our research. Size of the chosen segment is $a \times b$ and the thickness is $2h_0$. All edges are mechanically fixed. Ohm contacts are assumed at$x_1 = 0$ and a, while$x_3 = 0$ and b are electrically open. A voltage $\overline{\varphi}$ is applied at$x_1 = 0$, with $\overline{\varphi} = 0.4$V. The edge boundaries $x_3 = 0, b$ are thermally adiabatic, and $x_1 = 0, a$ maintain a constant temperature. The dimension of the chosen segment is kept at a microscale to sustain the assumption of small temperature perturbation. In addition, the loading areas are indicated by colored squares. The yellow region and green region are applied with opposite in-plane uniform mechanical loads $-t$ and t in the x_3-direction, respectively. Each loading area is a square with a side length of l and is distanced at $b/8$. The geometric parameters are as follows: $2h_0 = 50$nm, $a = 1.5\mu$m, $b = 6\mu$m and $l = 0.5\mu$m.

The boundary conditions of the research section can be displayed as:

$$
\begin{aligned}
&u = 0, \quad v = 0, \quad \varphi = \overline{\varphi}, \quad \Delta n = 0, \quad \theta = 0 \quad \text{at} \quad x_1 = 0,\\
&u = 0, \quad v = 0, \quad \varphi = 0, \quad \Delta n = 0, \quad \theta = 0 \quad \text{at} \quad x_1 = a,\\
&u = 0, \quad v = 0, \quad J_3 = 0, \quad D_3 = 0, \quad q_3 = 0 \quad \text{at} \quad x_3 = 0,\ b,\\
&\begin{cases}
\mathcal{F}_1 = 0, & \text{all segment},\\
\mathcal{F}_3 = t, & \text{in the green region},\\
\mathcal{F}_3 = -t, & \text{in the yellow region},\\
\mathcal{F}_3 = 0, & \text{in the white region}.
\end{cases}
\end{aligned}
\tag{18}
$$

As mentioned in Sect. 3.3, mechanical loads generate electrostatic potential barriers and wells, induce current redirection, and thereby affect the temperature fields. In the initial step of heating, to quickly heat the aimed object, we apply uniform mechanical forces in the negative x_3-direction in the yellow regions to induce potential barriers and opposite forces in the green regions to induce potential wells. Figure 11 shows the field distributions and currents under the action of symmetrical reaction loads $t = 3.5 \times 10^6$ N m^2 and an applied voltage $\overline{\varphi} = 0.4$V. In Figs. 11a and 12a, the arrows denote the current's magnitude and direction, with longer arrows indicating higher current densities. This visualization reveals that electron-generated currents

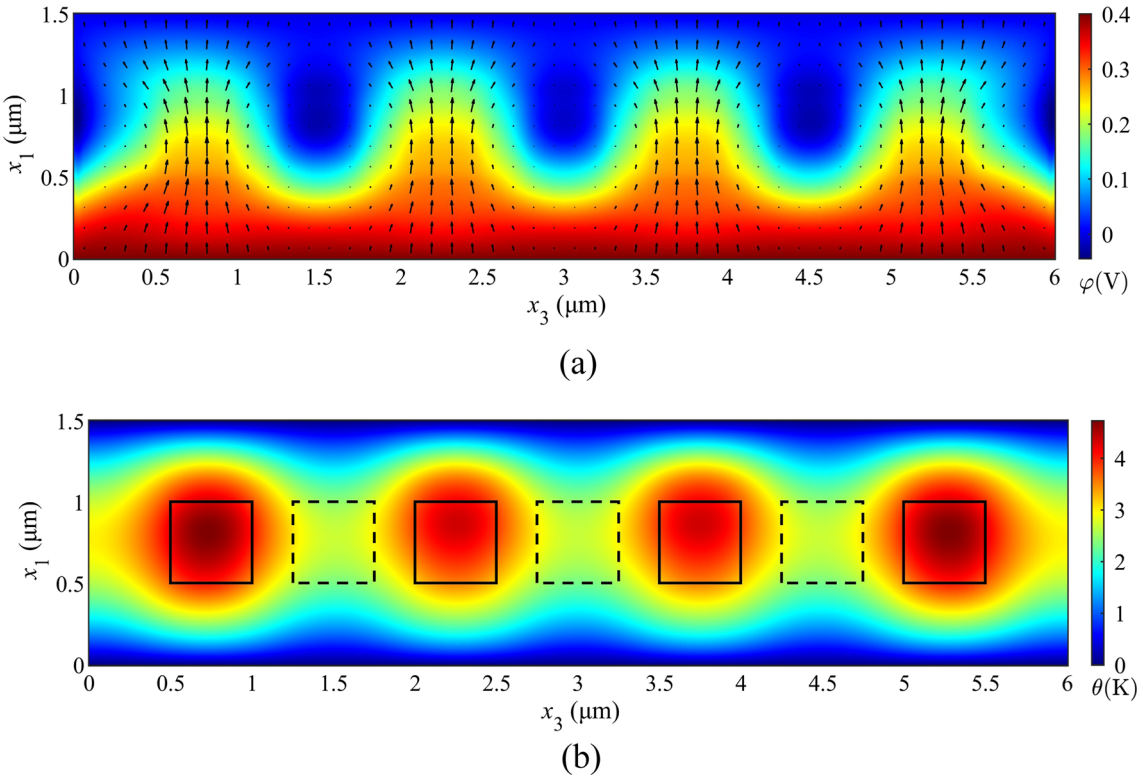

Fig. 11 Field distributions under the action of symmetrical reaction loads $t = 3.5 \times 10^6$ N m^{-2} and the voltage $\overline{\varphi} = 0.4$ V, **a** electrostatic potential and current density, which are indicated by the arrows. The length of the arrow represents the magnitude of the current density. **b** Temperature field

are drawn toward potential barriers, effectively circumventing the wells. This accumulation of current raises the temperature in these areas through the Joule heating effect. The average temperature of the solid square areas can reach up to 47.4% higher than the dotted square areas.

Once the targets are heated, we can apply reverse loads (i.e., $t = -3.5 \times 10^6$ N m^{-2}) to shift the heating area to the dotted square areas. As depicted in Fig. 12, the field distributions and current density differ from those shown in Fig. 11. By changing the magnitude of the mechanical forces, the temperature of the specified region can be effectively controlled. This strategy of periodic heating provides an easily controlled and uniform distribution of temperature fields, thereby reducing the risk of overheating and allowing for more efficient energy usage. In applications such as electronic devices or precision manufacturing, periodic thermal management can ensure safety and enhance product quality by maintaining optimal temperature conditions. For example, overheating can reduce efficiency in a computer chip, while periodic thermal control is essential for maintaining optimal chip temperatures and performance [57, 58]. Similarly, in 3D printing and semiconductor lithography and deposition, precise temperature control ensures material integrity in 3D printing and the fidelity of microstructures in semiconductor manufacturing, directly impacting product yield and quality. These examples highlight the importance of meticulous thermal management in high-precision technology applications.

5 Conclusion

This paper established a nonlinear model of thermo-piezo-elastic semiconductors that analyzes the response of thermo-electric fields under in-plane mechanical loads. Importantly, the model takes the performance of the thermoelectric effects into account in PSs, factors not considered in many previous studies. We interpret how external excitation affects the currents, and propose the possibility of thermal control by in-plane mechanical force.

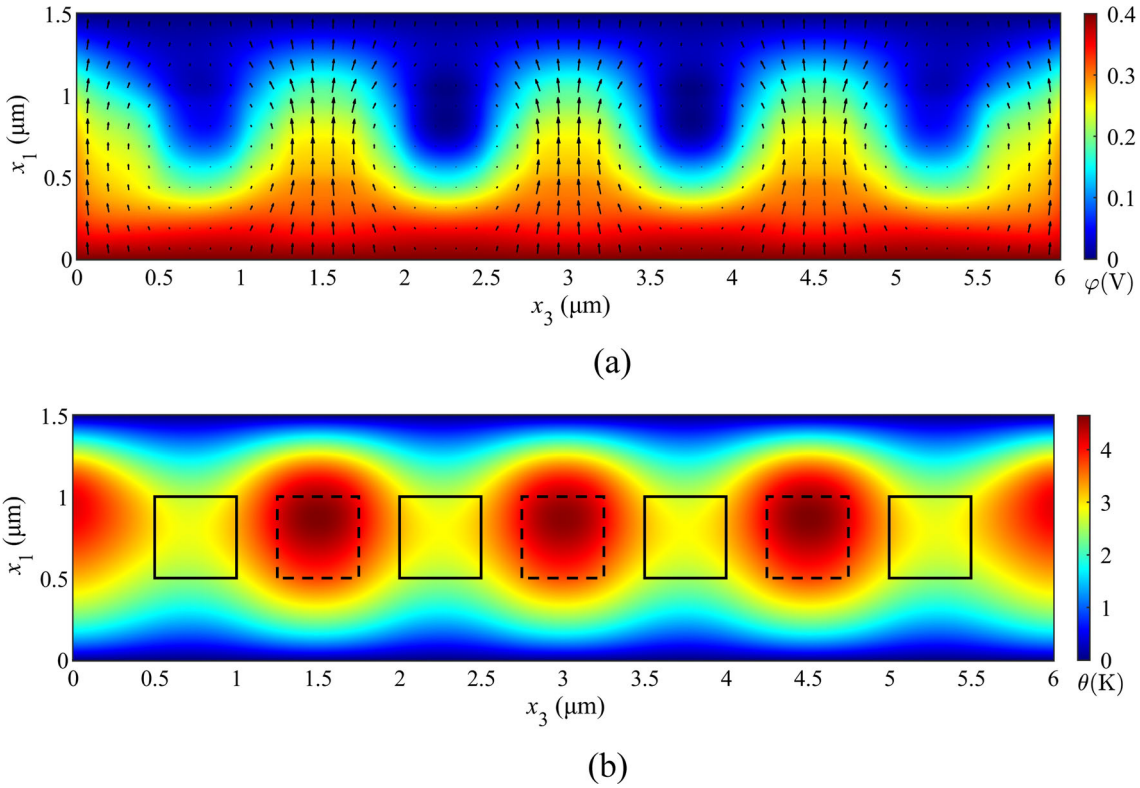

Fig. 12 Field distributions under the action of symmetrical reaction loads $t = -3.5 \times 10^6$ N m^{-2} and the voltage $\overline{\varphi} = 0.4$ V, **a** electrostatic potential and current density, which are indicated by the arrows. The length of the arrow represents the magnitude of the current density. **b** Temperature field

According to our study, a few novel phenomena with application potential can be observed from the numerical models:

1. When an in-plane mechanical load is applied to a PS film with an in-plane c-axis, it may induce local polarization, significantly influencing the currents and temperature field. The angle between the material's poling direction and the direction of the current significantly impacts the currents. In addition, when the currents run parallel to the c-axis, at an effective von Mises strain level of 0.01%, the magnitude of electric currents can be reduced by 70.4% compared to a scenario without any external forces.
2. This finding holds significant implications for devices that use PS materials as sensors. In addition, the temperature variation at the adiabatic boundary due to the heat fluxes generated by the thermoelectric effects can exhibit a substantial increase, reaching up to 4.6 times the value predicted under the assumption of pure Joule heat conditions. Furthermore, when the currents run perpendicular to the c-axis, external loads can cause temperature increases in regions with a high current density and decreases in regions with a low current density through piezoelectric coupling.
3. By applying mechanical loadings to a micro-heating device, it becomes possible to shift the main heating position to the desired locations. This mechanically induced current manipulation offers an effective way to control the temperature field within heating components. Such a method of thermal control is invaluable for safeguarding electronic components against thermal damage.

Acknowledgements This work was supported by the National Natural Science Foundation of China (Grant Nos. 12002086; 12072072) and Fundamental Research Funds for the Central Universities (Grant No. 2242022R40040).

Declarations

Conflict of interest The authors have no relevant financial or non-financial interests to disclose.

Appendix A: Validation of FE analysis

In this section, we aim to validate the accuracy of the results obtained from the FE analysis. We first linearize the nonlinear equations in Eq. (11) by removing the temperature as an independent variable. In the absence of an applied voltage on the boundaries, the Joule heating effect and Peltier effect vanish since no current is generated. For small Δn, we assume that the carrier concentration term in the drift current remains unchanged:

$$\theta \simeq 0, \quad J_i^n = qn\mu_{ij}^n(E_j - \alpha_{jk}^n\theta_{,k}) + qD_{ij}^n n_{,j} \simeq qn_0\mu_{ij}^n E_j + qD_{ij}^n \Delta n_{,j}. \tag{A.1}$$

Equation (11) can be linearized into

$$\begin{aligned}
&\bar{c}_{11}u_{,11} + \bar{c}_{13}v_{,31} + \bar{e}_{31}\varphi_{,31} + \bar{c}_{44}(u_{,33} + v_{,13}) + \bar{e}_{15}\varphi_{,13} + \frac{\mathcal{F}_1}{2h_0} = 0,\\
&\bar{c}_{44}(u_{,31} + v_{,11}) + \bar{e}_{15}\varphi_{,11} + \bar{c}_{13}u_{,13} + \bar{c}_{33}v_{,33} + \bar{e}_{33}\varphi_{,33} + \frac{\mathcal{F}_3}{2h_0} = 0,\\
&\bar{e}_{15}(u_{,31} + v_{,11}) - \bar{\varepsilon}_{11}\varphi_{,11} + \bar{e}_{31}u_{,13} + \bar{e}_{33}v_{,33} - \bar{\varepsilon}_{33}\varphi_{,33} = q(-\Delta n),\\
&-qn_0\mu_{11}^n\varphi_{,11} + qD_{11}^n(\Delta n)_{,11} - qn_0\mu_{33}^n\varphi_{,33} + qD_{33}^n(\Delta n)_{,33} = 0.
\end{aligned} \tag{A.2}$$

The planar model under in-plane mechanical loads is shown in Fig. 2. The geometric parameters in this section are: $2h_0 = 20\text{nm}$, $a = b = 1\mu\text{m}$ and$a_0 = b_0 = 0.2\mu\text{m}$.

The homogeneous boundary conditions, excluding thermal boundaries, are given by

$$\begin{aligned}
&v = 0, \quad T_{11} = 0, \quad \varphi = 0, \quad \Delta n = 0 \quad \text{at} \quad x_1 = 0,\ a,\\
&v = 0, \quad T_{13} = 0, \quad \varphi = 0, \quad \Delta n = 0 \quad \text{at} \quad x_3 = 0,\ b,\\
&\mathcal{F}_3 = \begin{cases} 10^6\text{N/m}^2, & \text{in} \quad \frac{a-a_0}{2} < x_1 < \frac{a+a_0}{2} \quad \text{and} \quad \frac{b-b_0}{2} < x_3 < \frac{b+b_0}{2},\\ 0, & \text{elsewhere.} \end{cases}
\end{aligned} \tag{A.3}$$

Given that only the displacement in the x_3-direction is constrained, the model is limited to applying mechanical force solely in the x_3-direction, implying $\mathcal{F}_1 = 0$. The Navier method is employed to solve the linear equations, and the field functions are expanded as trigonometric series to satisfy the boundary conditions in Eq. (A.3):

$$\begin{aligned}
u &= \sum_{m=0}^{\infty}\sum_{n=0}^{\infty} U_{mn}\cos(\xi_m x_1)\cos(\xi_n x_3),\\
v &= \sum_{m=0}^{\infty}\sum_{n=0}^{\infty} V_{mn}\sin(\xi_m x_1)\sin(\xi_n x_3),\\
\varphi &= \sum_{m=0}^{\infty}\sum_{n=0}^{\infty} \Psi_{mn}\sin(\xi_m x_1)\sin(\xi_n x_3),\\
\Delta n &= \sum_{m=0}^{\infty}\sum_{n=0}^{\infty} N_{mn}\sin(\xi_m x_1)\sin(\xi_n x_3),\\
\mathcal{F}_3 &= \sum_{m=0}^{\infty}\sum_{n=0}^{\infty} F_{mn}^{(3)}\sin(\xi_m x_1)\sin(\xi_n x_3),
\end{aligned} \tag{A.4}$$

where U_{mn},V_{mn}, Ψ_{mn} and N_{mn} are undetermined constants, and $F(3)$ mn is known from the given mechanical loads:

$$\begin{aligned}
F_{mn}^{(3)} &= \frac{4}{ab}\int_0^a\int_0^b \mathcal{F}_3\sin(\xi_m x_1)\sin(\xi_n x_3)\mathrm{d}x_1\mathrm{d}x_3,\\
\xi_m &= \frac{m\pi}{a}, \quad \xi_n = \frac{n\pi}{b}, \quad m,n = 1,\ 2,\ 3,\ \cdots.
\end{aligned} \tag{A.5}$$

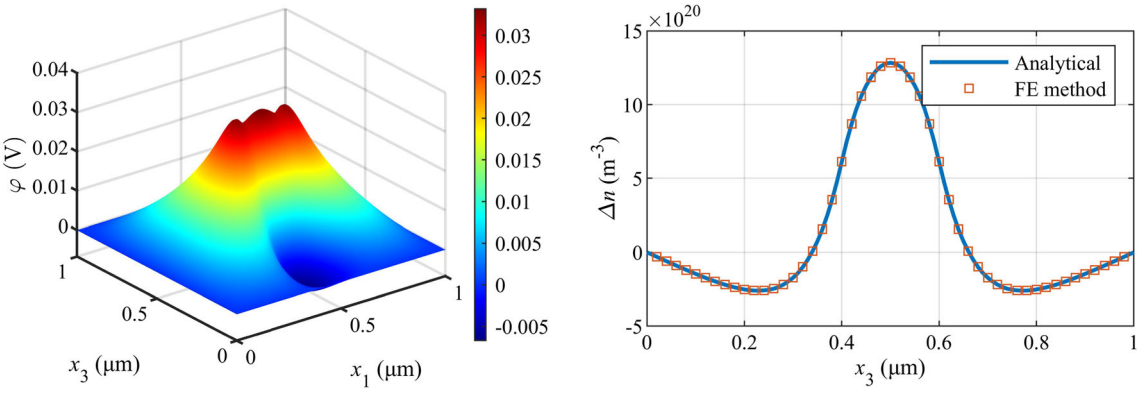

Fig. 13 Field distributions of an n-type doped ZnO film under mechanical loads, **a** electrostatic potential obtained from the analytical method and **b** comparison of perturbation of electron concentration with FE result along $x_1 = a/2$

Substituting Eq. (A.4) into Eq. (A.2) yields a system of linear algebraic equations for the undetermined constants:

$$\begin{aligned}
&U_{mn}(-\bar{c}_{11}\xi_m^2 - \bar{c}_{44}\xi_n^2) + V_{mn}(\bar{c}_{13}\xi_m\xi_n + c_{44}\xi_m\xi_n) + \Psi_{mn}(\bar{e}_{31}\xi_m\xi_n + \bar{e}_{15}\xi_m\xi_n) = 0,\\
&U_{mn}(\bar{c}_{44}\xi_m\xi_n + \bar{c}_{13}\xi_m\xi_n) + V_{mn}(-\bar{c}_{44}\xi_m^2 - \bar{c}_{33}\xi_n^2) + \Psi_{mn}(-\bar{e}_{15}\xi_m^2 - \bar{e}_{33}\xi_n^2) = -\frac{F_{mn}^{(3)}}{2h_0},\\
&U_{mn}(\bar{e}_{15}\xi_m\xi_n + \bar{e}_{31}\xi_m\xi_n) + V_{mn}(-\bar{e}_{15}\xi_m^2 - \bar{e}_{33}\xi_n^2) + \Psi_{mn}(\bar{\varepsilon}_{33}\xi_n^2 + \bar{\varepsilon}_{11}\xi_m^2) + qN_{mn} = 0,\\
&\Psi_{mn}(qn_0\mu_{11}^n\xi_m^2 + qn_0\mu_{33}^n\xi_n^2) + N_{mn}(-qD_{11}^n\xi_m^2 - qD_{33}^n\xi_n^2) = 0.
\end{aligned} \tag{A.6}$$

Figure 13a displays the distribution of electrostatic potential obtained from the analytical method. Figure 13b provides a comparative analysis of the analytical method with the FE result concerning the perturbation of electron concentration along $x_1 = a/2$, resulting in identical findings with the analytical result. In an n-type doped semiconductor, where electrons are abundant, carriers tend to accumulate in areas of high electrostatic potential. Therefore, the distributions of electrons and electrostatic potential are in complete agreement. By comparing the numerical results from the FE method with the analytical solutions for the reduced linear case, the accuracy of the FE results is verified.

References

1. Zhu, Q., Wu, T., Wang, N.: From piezoelectric nanogenerator to non-invasive medical sensor: a review. Biosensors (2023). https://doi.org/10.3390/bios13010113
2. Deng, W., Zhou, Y., Libanori, A., et al.: Piezoelectric nanogenerators for personalized healthcare. Chem. Soc. Rev. **51**(9), 3380–3435 (2022). https://doi.org/10.1039/d1cs00858g
3. Hickernell, F.S.: The piezoelectric semiconductor and acoustoelectronic device development in the sixties. IEEE Trans. Ultrason. Ferroelectr. Freq. Control **52**(5), 737–745 (2005). https://doi.org/10.1109/TUFFC.2005.1503961
4. Haq, M.: Application of piezo transducers in biomedical science for health monitoring and energy harvesting problems. Mater. Res. Express **6**(2), 022002 (2018). https://doi.org/10.1088/2053-1591/aaefb8
5. Liu, H., Lin, X., Zhang, S., et al.: Enhanced performance of piezoelectric composite nanogenerator based on gradient porous PZT ceramic structure for energy harvesting. J. Mater. Chem. A **8**(37), 19631–19640 (2020). https://doi.org/10.1039/d0ta03054f
6. Chen, S., Li, J., Song, Y., et al.: Flexible and environment-friendly regenerated cellulose/MoS 2 nanosheet nanogenerators with high piezoelectricity and output performance. Cellulose **28**, 6513–6522 (2021). https://doi.org/10.1007/s10570-021-03962-z
7. Cao, X., Xiong, Y., Sun, J., et al.: Piezoelectric nanogenerators derived self-powered sensors for multifunctional applications and artificial intelligence. Adv. Func. Mater. **31**(33), 2102983 (2021). https://doi.org/10.1002/adfm.202102983
8. Zhou, X., Parida, K., Halevi, O., et al.: All 3D printed stretchable piezoelectric nanogenerator for self-powered sensor application. Sensors (2020). https://doi.org/10.3390/s20236748
9. Hu, D., Yao, M., Fan, Y., et al.: Strategies to achieve high performance piezoelectric nanogenerators. Nano Energy **55**, 288–304 (2019). https://doi.org/10.1016/j.nanoen.2018.10.053
10. Altowireb, S.M., Goumri-Said, S.: Core--shell structures for the enhancement of energy harvesting in piezoelectric Nanogenerators: a review. Sustain. Energy Technol. Assess. **55**, 102982 (2023). https://doi.org/10.1016/j.seta.2022.102982

11. Su, H., Wang, X., Li, C., et al.: Enhanced energy harvesting ability of polydimethylsiloxane-BaTiO3-based flexible piezoelectric nanogenerator for tactile imitation application. Nano Energy **83**, 105809 (2021). https://doi.org/10.1016/j.nanoen.2021.105809
12. Novak, N., Keil, P., Frömling, T., et al.: Influence of metal/semiconductor interface on attainable piezoelectric and energy harvesting properties of ZnO. Acta Mater. **162**, 277–283 (2019). https://doi.org/10.1016/j.actamat.2018.10.008
13. Li, S.: On global energy release rate of a permeable crack in a piezoelectric ceramic. J. Appl. Mech. **70**(2), 246–252 (2003). https://doi.org/10.1115/1.1544539
14. Li, S.: The electromagneto-acoustic surface wave in a piezoelectric medium: the Bleustein-Gulyaev mode. J. Appl. Phys. **80**(9), 5264–5269 (1996). https://doi.org/10.1063/1.363466
15. He, J., Du, J., Yang, J.: Stress effects on electric currents in antiplane problems of piezoelectric semiconductors over a rectangular domain. Acta Mech. **233**(3), 1173–1185 (2022). https://doi.org/10.1007/s00707-022-03148-z
16. Qu, Y., Jin, F., Yang, J.: Electromechanical interactions in a composite plate with piezoelectric dielectric and nonpiezoelectric semiconductor layers. Acta Mech. **233**(9), 3795–3812 (2022). https://doi.org/10.1007/s00707-022-03309-0
17. Liu, D., Fang, K., Li, P., et al.: Electromechanical field analysis of PN junctions in bent composite piezoelectric semiconductor beams under shear forces. Acta Mech. (2023). https://doi.org/10.1007/s00707-023-03790-1
18. Pan, C., Zhai, J., Wang, Z.L.: Piezotronics and piezo-phototronics of third generation semiconductor nanowires. Chem. Rev. **119**(15), 9303–9359 (2019). https://doi.org/10.1021/acs.chemrev.8b00599
19. Wu, W., Wang, Z.L.: Piezotronics and piezo-phototronics for adaptive electronics and optoelectronics. Nat. Rev. Mater. **1**(7), 1–17 (2016). https://doi.org/10.1038/natrevmats.2016.31
20. Wang, Z.L.: Piezopotential gated nanowire devices: piezotronics and piezo-phototronics. Nano Today **5**(6), 540–552 (2010). https://doi.org/10.1016/j.nantod.2010.10.008
21. Yang, G., Yang, L., Du, J., et al.: PN junctions with coupling to bending deformation in composite piezoelectric semiconductor fibers. Int. J. Mech. Sci. **173**, 105421 (2020). https://doi.org/10.1016/j.ijmecsci.2020.105421
22. Fang, K., Qian, Z., Yang, J.: Piezopotential in a composite cantilever of piezoelectric dielectrics and nonpiezoelectric semiconductors produced by shear force through e 15. Mater. Res. Express **6**(11), 115917 (2019). https://doi.org/10.1088/2053-1591/ab4bf5
23. Huang, H., Qian, Z., Yang, J.: I-V characteristics of a piezoelectric semiconductor nanofiber under local tensile/compressive stress. J. Appl. Phys. (2019). https://doi.org/10.1063/1.5110876
24. Qu, Y., Jin, F., Yang, J.: Stress-induced electric potential barriers in thickness-stretch deformations of a piezoelectric semiconductor plate. Acta Mech. **232**(11), 4533–4543 (2021). https://doi.org/10.1007/s00707-021-03059-5
25. Guo, Z., Chen, J., Zhang, G., et al.: Exact solutions for plane stress problems of piezoelectric semiconductors: tuning free-carrier motions by various mechanical loadings. Eur. J. Mech. A. Solids (2023). https://doi.org/10.1016/j.euromechsol.2023.105073
26. Qu, Y., Jin, F., Yang, J.: Torsion of a piezoelectric semiconductor rod of cubic crystals with consideration of warping and in-plane shear of its rectangular cross section. Mech. Mater. **172**, 104407 (2022). https://doi.org/10.1016/j.mechmat.2022.104407
27. Zhao, M., Ma, Z., Lu, C., et al.: Application of the homopoty analysis method to nonlinear characteristics of a piezoelectric semiconductor fiber. Appl. Math. Mech. **42**(5), 665–676 (2021). https://doi.org/10.1007/s10483-021-2726-5
28. Fang, K., Li, P., Li, N., et al.: Model and performance analysis of non-uniform piezoelectric semiconductor nanofibers. Appl. Math. Model. **104**, 628–643 (2022). https://doi.org/10.1016/j.apm.2021.12.009
29. Nolas, G.S., Sharp, J., Goldsmid, J.: Thermoelectrics: basic principles and new materials developments, pp. 1-14. Springer, Berlin, Heidelberg (2001). https://doi.org/10.1007/978-3-662-04569-5
30. Eslami, M.R., Hetnarski, R.B., Ignaczak, J., et al.: Theory of elasticity and thermal stresses, pp. 353-355. Springer, Dordrecht (2013). https://doi.org/10.1007/978-94-007-6356-2
31. Oh, H., Dayeh, S.A.: Physics-based device models and progress review for active piezoelectric semiconductor devices. Sensors (2020). https://doi.org/10.3390/s20143872
32. Sladek, J., Sladek, V., Repka, M., et al.: A novel gradient theory for thermoelectric material structures. Int. J. Solids Struct. **206**, 292–303 (2020). https://doi.org/10.1016/j.ijsolstr.2020.09.023
33. Song, K., Yin, D., Schiavone, P.: Thermal-electric-elastic analyses of a thermoelectric material containing two circular holes. Int. J. Solids Struct. **213**, 111–120 (2021). https://doi.org/10.1016/j.ijsolstr.2020.12.019
34. Luo, Y., Zhang, C., Chen, W., et al.: Thermally induced electromechanical fields in unimorphs of piezoelectric dielectrics and nonpiezoelectric semiconductors. Integr. Ferroelectr. **211**(1), 117–131 (2020). https://doi.org/10.1080/10584587.2020.1803680
35. Qu, Y., Jin, F., Yang, J.: Temperature effects on mobile charges in thermopiezoelectric semiconductor plates. Int. J. Appl. Mech. (2021). https://doi.org/10.1142/s175882512150037x
36. Zhang, G.Y., Guo, Z.W., Qu, Y.L., et al.: A new model for thermal buckling of an anisotropic elastic composite beam incorporating piezoelectric, flexoelectric and semiconducting effects. Acta Mech. **233**(5), 1719–1738 (2022). https://doi.org/10.1007/s00707-022-03186-7
37. Carraro, P.A., Pontefisso, A., Quaresimin, M.: Modelling the thermoelectric behaviour of composite laminates in the presence of transverse cracks. Appl. Math. Model. **115**, 568–583 (2023). https://doi.org/10.1016/j.apm.2022.10.046
38. Zhao, L., Gu, S., Song, Y., et al.: Transient analysis on surface heated piezoelectric semiconductor plate lying on rigid substrate. Appl. Math. Mech. **43**(12), 1841–1856 (2022). https://doi.org/10.1007/s10483-022-2927-6
39. Yang, Z., Sun, L., Zhang, C., et al.: Analysis of a composite piezoelectric semiconductor cylindrical shell under the thermal loading. Mech. Mater. **164**, 104153 (2022). https://doi.org/10.1016/j.mechmat.2021.104153
40. Qu, Y.L., Zhang, G.Y., Gao, X.L., et al.: A new model for thermally induced redistributions of free carriers in centrosymmetric flexoelectric semiconductor beams. Mech. Mater. (2022). https://doi.org/10.1016/j.mechmat.2022.104328
41. Song, Y., Li, S., Li, Y.: Peridynamic modeling and simulation of thermo-mechanical fracture in inhomogeneous ice. Eng. Comput. **39**(1), 575–606 (2023). https://doi.org/10.1007/s00366-022-01616-7

42. Qu, Y., Pan, E., Zhu, F., et al.: Modeling thermoelectric effects in piezoelectric semiconductors: new fully coupled mechanisms for mechanically manipulated heat flux and refrigeration. Int. J. Eng. Sci. **182**, 10 (2023). https://doi.org/10.1016/j.ijengsci.2022.103775
43. Li, J.-F., Liu, W.-S., Zhao, L.-D., et al.: High-performance nanostructured thermoelectric materials. NPG Asia Mater. **2**(4), 152–158 (2010). https://doi.org/10.1038/asiamat.2010.138
44. Liu, L.: A continuum theory of thermoelectric bodies and effective properties of thermoelectric composites. Int. J. Eng. Sci. **55**, 35–53 (2012). https://doi.org/10.1016/j.ijengsci.2012.02.003
45. Zhang, L., Shi, X.-L., Yang, Y.-L., et al.: Flexible thermoelectric materials and devices: from materials to applications. Mater. Today **46**, 62–108 (2021). https://doi.org/10.1016/j.mattod.2021.02.016
46. Shi, P., Qin, W., Li, X., et al.: Thermoelectric conversion efficiency of a two-dimensional thermoelectric plate of finite-size with a center crack. Acta Mech. **233**(11), 4785–4803 (2022). https://doi.org/10.1007/s00707-022-03348-7
47. Reddy J N: Theory and analysis of elastic plates and shells, pp. 18–32 (2006). https://doi.org/10.1201/9780849384165
48. Pierret R F: Semiconductor device fundamentals, pp. 1–51. Addison-Wesley (1996)
49. Qu, Y., Jin, F., Yang, J.: Temperature-induced potential barriers in piezoelectric semiconductor films through pyroelectric and thermoelastic couplings and their effects on currents. J. Appl. Phys. (2022). https://doi.org/10.1063/5.0083759
50. Hahn, D.W., Özisik, M.N.: Heat conduction, pp. 2–11. John Wiley & Sons (2012). https://doi.org/10.1002/9781118411285
51. Jin, Z.-H., Yang, J.: Analysis of a sandwiched piezoelectric semiconducting thermoelectric structure. Mech. Res. Commun. **98**, 31–36 (2019). https://doi.org/10.1016/j.mechrescom.2019.05.004
52. Ibach, H.: Thermal expansion of silicon and zinc oxide (I). Physica Status Solidi (b) **31**(2), 625–634 (1969). https://doi.org/10.1002/pssb.19690310224
53. Nah, J.J., Kang, H.G., Huh, M.Y., et al.: Effect of strain states during cold rolling on the recrystallized grain size in an aluminum alloy. Scr. Mater. **58**(6), 500–503 (2008). https://doi.org/10.1016/j.scriptamat.2007.10.049
54. Carraro, P.A., Maragoni, L., Paipetis, A.S., et al.: Prediction of the Seebeck coefficient of thermoelectric unidirectional fibre-reinforced composites. Compos. Part B Eng. (2021). https://doi.org/10.1016/j.compositesb.2021.109111
55. Guo, M., Lu, C., Qin, G., et al.: Temperature gradient-dominated electrical behaviours in a piezoelectric PN junction. J. Electron. Mater. **50**(3), 947–953 (2021). https://doi.org/10.1007/s11664-020-08634-5
56. Zhang, X., Hou, Y., Yang, Y., et al.: Stamp-like energy harvester and programmable information encrypted display based on fully printable thermoelectric devices. Adv. Mater. (2022). https://doi.org/10.1002/adma.202207723
57. Lankry, A., Koyfman, A., Haustein, H.D., et al.: Onset of heterogeneous nucleation in pool boiling of HFE-7100 following rapid heating on a microscale heater. Exp. Therm. Fluid Sci. **152**, 111125 (2024). https://doi.org/10.1016/j.expthermflusci.2023.111125
58. Zheng, Z., Xu, H., Wen, J., et al.: In-situ growth of diamond/Ag as hybrid filler for enhancing thermal conductivity of liquid crystal epoxy. Diam. Relat. Mater. **141**, 110659 (2024). https://doi.org/10.1016/j.diamond.2023.110659